Linear–Quadratic Mixing Model for Reflectances in Urban Environments

Inès Meganem, Philippe Déliot, Xavier Briottet, Yannick Deville, *Member, IEEE*, and Shahram Hosseini

***Abstract*—In the field of remote sensing, the unmixing of hyperspectral images is usually based on the use of a mixing model. Most existing spectral unmixing methods, used in the reflective range (0.4–2.5 μm), rely on a linear model of endmember reflectances. Nevertheless, such a model supposes the pixels at the ground level to be uniformly irradiated and the scene to be flat. When considering a 3-D landscape, such a model is no longer valid as irradiated and shadowed areas are present, as well as radiative interactions between facing surfaces. This paper introduces a new mixing model adapted to urban environments and which aims to overcome these limitations. This model is derived from physical equations based on radiative transfer theory, and its analytic expression is linear–quadratic. Similar models have already been used in the literature for unmixing purposes but without being justified by physical analysis. Our proposed model is validated using a synthetic but realistic European 3-D urban scene. Then, simplifications are introduced, based on a study of the different radiative components contributing to the signal in a way to make the model easy to use for spectral unmixing. This paper also shows that the quadratic term cannot be neglected in many cases in urban environments since it can, e.g., range from 15% to 20% of the reflectances in canyons.**

***Index Terms*—Linear–quadratic mixing model, physical modeling, reflectances, spectral unmixing, urban images.**

I. Introduction

BECAUSE of the low spatial resolution of hyperspectral image sensors compared to panchromatic ones, a pixel rarely represents a homogeneous surface, and the signal incident to a sensor into its instantaneous field of view (IFOV) often results from contributions of several materials. For example, in [1], the authors found that, in HyMap images acquired over Dresden, Germany, 52% of the pixels comprise spectral mixtures. In the case of mixed pixels, it is possible to retrieve the constituent components of a given pixel using spectral mixture analysis techniques owing to the spectral richness of the data. This process of subpixel retrieval is called spectral unmixing.

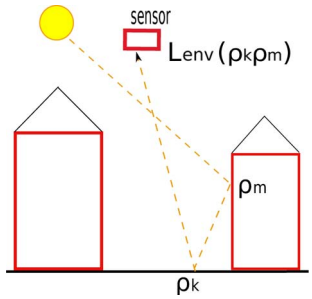

Fig. 1. Contribution of the reflections due to the neighborhood, with ρ_i denoting the reflectance of surface i (where i can be k or m) and L_{env} denoting the radiance due to these reflections.

Our work is focused on the reflective domain (wavelengths from 0.4 to 2.5 μm). Most available unmixing methods in this domain rely on linear mixing models for reflectances (see, e.g., [2]–[9] and the references therein), where the mixing coefficients are the abundances. Such an assumption is valid when the scene is flat with a homogeneous incident irradiance.

In this paper, we aim at deriving a mixing model of reflectances adapted to urban images. This involves a more complicated model because towns are characterized by a high spatial variability at a meter scale which implies different illumination levels (sunny and shadowed areas). Moreover, the 3-D structure of such environments induces multiple scatterings of light between surfaces (see Fig. 1). As a consequence, the reflectance of one pixel can contain the contribution of a material reflectance from its neighborhood, even if the surface represented by the pixel does not contain this material. Then, the linear model is no longer valid since this model assumes that only the content of the pixel contributes to its reflectance.

Taking into account multiple reflections of light between surfaces yields a nonlinear model. Nonlinearity in unmixing has been considered in previous works (e.g., [10]–[13]), where the proposed methods essentially make use of neural networks. However, these methods are presented without an explicit mixing model. These papers show though that considering possible nonlinearities in the model improves unmixing performance. In [14], the experimental results obtained with an image acquired in a laboratory (from a synthetic scene) showed that a second-order model better describes the mixtures than a linear one, in

Manuscript received May 9, 2012; revised October 6, 2012 and December 21, 2012; accepted December 22, 2012. Date of publication March 13, 2013; date of current version November 26, 2013.

I. Meganem is with the ONERA "The French Aerospace Lab", 31055 Toulouse, France, and also with the Institut de Recherche en Astrophysique et Planétologie (IRAP), Observatoire Midi-Pyrénées, Université Paul Sabatier, University of Toulouse–National Centre for Scientific Research (CNRS), 31400 Toulouse, France (e-mail: meganem@irap.omp.eu).

P. Déliot and X. Briottet are with the Theoretical and Applied Optics Department (DOTA), ONERA "The French Aerospace Lab", 31055 Toulouse, France (e-mail: philippe.deliot@onera.fr; xavier.briottet@onera.fr).

Y. Deville and S. Hosseini are with the Institut de Recherche en Astrophysique et Planétologie, Observatoire Midi-Pyrénées, Université Paul Sabatier, University of Toulouse–National Centre for Scientific Research (CNRS), 31400 Toulouse, France (e-mail: yannick.deville@irap.omp.eu; shahram.hosseini@irap.omp.eu).

Color versions of one or more of the figures in this paper are available online at http://ieeexplore.ieee.org.

Digital Object Identifier 10.1109/TGRS.2013.2242475

the case of 3-D structures like in urban environments, since it gives more accurate unmixing results.

Starting from physical equations based on radiative transfer theory, we derive a new physically based mixing model that deals with the nonlinearities faced in urban environments. The derived linear–quadratic model only takes into account second-order reflections, neglecting higher order interactions, which is very realistic given the range of values for reflectances (values between zero and one). Similar models were used in some unmixing approaches in the literature, for different types of scenes, but without any physical justification: orchards [15], [16], forests [17], and scenes composed of vegetation, water, and soil materials [18]. The assumptions made on the mixing coefficients are not either physically justified in those works. In this paper, we propose the justification and validation of the linear–quadratic model in the presence of 3-D structures. A substantiation of the possible assumptions concerning the mixing coefficients is also given. This work thus aims at giving a realistic model that could be used for unmixing methods.

In Section II, the method used to derive our physical mixing model for urban scenes is explained. This model is then validated in Section III, and the relative impact of radiative terms is evaluated, based on synthetic images. In Section IV, simplifications of this model, using reasonable assumptions, are presented. This yields an invariant instantaneous linear–quadratic mixing model. Eventually, in Section V, we finalize this model to make it more convenient for spectral unmixing. We also discuss the possible assumptions on the mixing coefficients, compared to what exists in the literature.

II. Physical Mixing Model

In this section, we show how our physical mixing model is derived, starting from physical equations based on radiative transfer theory. The development of this model followed the same procedure as in [19], developed in the thermal infrared domain. The approach, originally proposed in [20], consists in comparing the sensor radiance at a coarse resolution with all the radiance coming from the different elementary surfaces inside the coarse pixel.

A. Presentation of the Method Leading to the Model

At a coarse resolution, a pixel often corresponds to a heterogeneous surface composed of different elementary homogeneous surfaces. Thus, for each pixel, the sensor receives contributions resulting from reflectances of all these elementary surfaces. This is illustrated in Fig. 2(a). However, the signal received by the sensor from this heterogeneous surface can be considered as the resulting signal coming from an equivalent horizontal homogeneous flat surface. We thus assume that, at a coarse resolution, each pixel of the image can be associated with such a flat equivalent surface at the height of the urban canopy. Therefore, we attribute an equivalent reflectance $\langle\rho\rangle$ (corresponding to the flat equivalent surface) to this pixel [see Fig. 2(b)]. Then, to derive the equation expressing the equivalent reflectance of a pixel as a function of the contributions

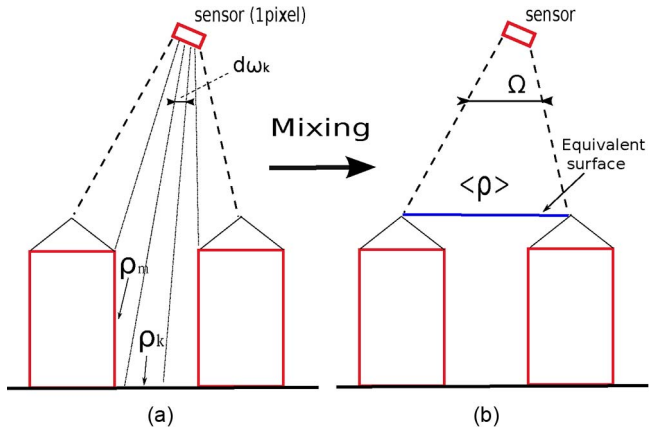

Fig. 2. Mixing principle - the dashed lines define the coarse IFOV Ω, and the continuous lines define the fine IFOV $d\omega_k$.

of elementary surface reflectances, the following method is applied.

1) Express the total radiance of a given pixel as the result of the contributions of the different materials composing it at the ground level (Section II-B).
2) Express the radiance of a pixel considering its associated equivalent surface (Section II-C).
3) Perform a term-by-term radiative identification of the two preceding expressions to derive the equivalent reflectance expression for the pixel (Section II-D).

B. Radiance From the Ground Level at a Fine Scale

Assuming that each pixel is composed of N homogeneous elementary surfaces indexed by k, the total radiance L_{mix} received by the sensor, in the field of view delimited by the solid angle Ω corresponding to a given pixel, can be expressed as

$$\begin{aligned}\Omega L_{\text{mix}} = &\sum_k L_{D,k} d\omega_k + \sum_k L^{\downarrow}_{\text{atm},k} d\omega_k \\ &+ \sum_k L_{\text{env},k} d\omega_k + \sum_k L_{\text{coupling},k} d\omega_k \\ &+ \sum_k L^{\uparrow}_{\text{atm},k} d\omega_k + \sum_k L^{\uparrow}_{\text{diff},k} d\omega_k \end{aligned} \quad (1)$$

where

- $d\omega_k$ solid angle corresponding to an elementary surface k;
- $L_{D,k}$ solar radiance due to the solar irradiance on the surface k directly reflected toward the sensor;
- $L^{\downarrow}_{\text{atm},k}$ atmospheric downwelling radiance incident on the surface k and directly transmitted toward the sensor;
- $L_{\text{env},k}$ radiance due to the neighborhood of the considered surface k;
- $L_{\text{coupling},k}$ radiance due to multiple scatterings between the atmosphere and the ground;
- $L^{\uparrow}_{\text{diff},k}$ radiance due to the total downwelling irradiance, incident on the neighborhood of the surface k and reflected toward the sensor direction;

$L^{\uparrow}_{\mathrm{atm},k}$ upwelling atmospheric radiance, reaching the sensor in the solid angle $d\omega_k$.

By replacing the radiances of interest by their expressions given in [21], this yields

$$\begin{aligned} L_{\mathrm{mix}} = &\sum_k S_k t^{\uparrow k-c} \frac{\rho_k^{dd}(\overrightarrow{U_s}, \overrightarrow{U_{c,k}})}{\pi} E_{D,k} + \sum_k S_k L^{\downarrow}_{\mathrm{atm},k} \\ &+ \sum_k S_k t^{\uparrow k-c} \int\int_{m\in V_k} \frac{\rho_k^{dd}(\overrightarrow{U_{km}}, \overrightarrow{U_{c,k}})}{\pi} g_{m,k} \\ &\quad \times \left[\frac{\rho_m^{dd}(\overrightarrow{U_s}, \overrightarrow{U_{mk}})}{\pi} E_{D,m} + \frac{\rho_m^{hd}(\overrightarrow{U_{mk}})}{\pi} E_{\mathrm{diff},m} \right] dS_m \\ &+ \sum_k S_k L_{\mathrm{coupling},k} + \sum_k S_k L^{\uparrow}_{\mathrm{atm},k} \\ &+ \sum_k S_k L^{\uparrow}_{\mathrm{diff},k} \end{aligned} \tag{2}$$

where

$S_k = d\omega_k/\Omega$ normalized elementary solid angle over which the sensor sees an elementary surface k (with $\sum_k S_k = 1$);

$t^{\uparrow k-c}$ atmospheric transmission from surface k up to the sensor;

$\overrightarrow{U_s}$ normalized vector of the sun's direction at surface k;

$\overrightarrow{U_{c,k}}$ normalized vector of the sensor's direction with respect to surface k;

$\overrightarrow{U_{km}}$ normalized vector defining the direction between surface k and surface m (vector linking the centers of these surfaces);

ρ_k^{dd} bidirectional reflectance of elementary surface k, with the directions being defined by $\overrightarrow{U_s}$ and $\overrightarrow{U_{c,k}}$ (unitless);

ρ_k^{hd} hemispheric directional reflectance of surface k depending only on the observation direction (unitless);

$E_{D,k}$ direct solar irradiance on surface k;

$E_{\mathrm{diff},m}$ atmospheric irradiance on surface m;

V_k neighborhood of surface k;

$g_{m,k} = \langle \overrightarrow{n_k}, \overrightarrow{U_{km}} \rangle \cdot (\langle \overrightarrow{n_m}, \overrightarrow{U_{mk}} \rangle / r^2)$ geometric factor (named so because it only depends on the geometry of the scene), where r is the distance between surfaces m and k and $\overrightarrow{n_k}$ is normal to surface k.

Note that ρ_k^{hd}, ρ_k^{dd}, and all the reflectances considered in this work are defined as in [22]; they are thus unitless.

C. Radiance From the Equivalent Surface Level

Let $\langle L \rangle$ be the equivalent radiance corresponding to the equivalent surface, defined at the height of the urban canopy, and associated with our pixel. This equivalent radiance $\langle L \rangle$ is the radiance measured by a sensor viewing a flat surface

$$\begin{aligned} \langle L \rangle &= \langle L_{\mathrm{es}} \rangle + L^{\downarrow}_{\mathrm{atm}} + L_{\mathrm{coupling}} + L^{\uparrow \mathrm{es}-c}_{\mathrm{atm}} + L^{\uparrow}_{\mathrm{diff}} \\ &= \frac{\langle \rho \rangle}{\pi} E_D t^{\uparrow \mathrm{es}-c} + L^{\downarrow}_{\mathrm{atm}} + L_{\mathrm{coupling}} + L^{\uparrow \mathrm{es}-c}_{\mathrm{atm}} + L^{\uparrow}_{\mathrm{diff}} \end{aligned} \tag{3}$$

where $\langle L_{\mathrm{es}} \rangle$ is the radiance at the equivalent surface level resulting from the reflection of solar irradiance on the equivalent surface. $L^{\uparrow \mathrm{es}-c}_{\mathrm{atm}}$ and $t^{\uparrow \mathrm{es}-c}$ are the atmospheric upwelling radiance and transmission from the equivalent surface toward the sensor, respectively. All other terms are the same as those in (2) except that they are here defined at the equivalent surface level (and not for an elementary surface on the ground).

As we can see, the terms due to the environment are not present here [compared to (2)] because the surface is flat.

The atmospheric upwelling transmission and the atmospheric upwelling radiance in (2) can be expressed as functions of those in (3)

$$t^{\uparrow k-c} = t^{\uparrow k-\mathrm{es}} \times t^{\uparrow \mathrm{es}-c} \tag{4}$$

$$\begin{aligned} \sum_k S_k L^{\uparrow}_{\mathrm{atm},k} &= \sum_k S_k L^{\uparrow k-c}_{\mathrm{atm},k} \\ &= \sum_k S_k L^{\uparrow k-\mathrm{es}}_{\mathrm{atm},k} \times t^{\uparrow \mathrm{es}-c} + L^{\uparrow \mathrm{es}-c}_{\mathrm{atm}} \end{aligned} \tag{5}$$

where $t^{\uparrow k-\mathrm{es}}$ is the atmospheric upwelling transmission from a surface k to the equivalent surface and $L^{\uparrow k-\mathrm{es}}_{\mathrm{atm}}$ is the atmospheric upwelling radiance from surface k toward the equivalent surface.

D. Identification Leading to the Mixing Model

The total radiance expressions for a pixel defined in (2) and (3) are equal, i.e., $L_{\mathrm{mix}} = \langle L \rangle$. Thus, considering the physical conservation of radiant flux at every scale, a term-by-term identification is performed. By identifying the radiative terms of the same nature in these two expressions, we can easily eliminate the following terms: $L^{\downarrow}_{\mathrm{atm}}$, L_{coupling}, and $L^{\uparrow}_{\mathrm{diff}}$. Using (5), the term $L^{\uparrow \mathrm{es}-c}_{\mathrm{atm}}$ can also be eliminated. This leads to

$$\begin{aligned} \frac{\langle \rho \rangle}{\pi} E_D t^{\uparrow \mathrm{es}-c} = &\sum_k S_k t^{\uparrow k-c} \frac{\rho_k^{dd}(\overrightarrow{U_s}, \overrightarrow{U_{c,k}})}{\pi} E_{D,k} \\ &+ \sum_k S_k t^{\uparrow k-c} \int\int_{m\in V_k} \frac{\rho_k^{dd}(\overrightarrow{U_{km}}, \overrightarrow{U_{c,k}})}{\pi} g_{m,k} \\ &\quad \times \left[\frac{\rho_m^{dd}(\overrightarrow{U_s}, \overrightarrow{U_{mk}})}{\pi} E_{D,m} \right. \\ &\qquad \left. + \frac{\rho_m^{hd}(\overrightarrow{U_{mk}})}{\pi} E_{\mathrm{diff},m} \right] dS_m \\ &+ \sum_k S_k L^{\uparrow k-\mathrm{es}}_{\mathrm{atm},k} \times t^{\uparrow \mathrm{es}-c}. \end{aligned} \tag{6}$$

We then eliminate $t^{\uparrow \mathrm{es}-c}$, in all terms, using (4). The last terms $L^{\uparrow k-\mathrm{es}}_{\mathrm{atm},k}$ can be removed, considering that the atmosphere between the ground and the urban canopy can be neglected. For the same reason, the atmospheric transmission under the

canopy level is $t^{\uparrow k-\mathrm{es}} \simeq 1$ (assuming that we are outside a strong absorption band). We can finally express the equivalent reflectance of a pixel as a function of the elementary reflectances

$$\langle\rho\rangle = \sum_{k=1}^{N} S_k \left[\rho_k^{dd}(\overrightarrow{U_s}, \overrightarrow{U_{c,k}}) \frac{E_{D,k}}{E_D} + \int\int_{m\in V_k} \rho_k^{dd}(\overrightarrow{U_{km}}, \overrightarrow{U_{c,k}}) g_{m,k} \times \left(\frac{\rho_m^{dd}(\overrightarrow{U_s}, \overrightarrow{U_{mk}})}{\pi} \frac{E_{D,m}}{E_D} + \frac{\rho_m^{hd}(\overrightarrow{U_{mk}})}{\pi} \frac{E_{\mathrm{diff},m}}{E_D} \right) dS_m \right]. \quad (7)$$

Note that this equation is valid for a pixel totally or partially in the sun ($E_D \neq 0$).

We now assume, without loss of generality, that reflectances have a Lambertian behavior in the second additive term (ρ_k and ρ_m do not depend on the sun and sensor directions: $\rho^{hd} = \rho^{dd} = \rho$). This assumption is possible because multiple reflections tend to make the material behavior Lambertian and because this term is small compared to the first one. The reflectances in the latter are therefore denoted ρ_k and ρ_m. We also approximate the integrals by sums assuming that the neighborhood of an elementary surface k is composed of elementary surfaces m of area ΔS and each one is made up of only one material. This yields

$$\langle\rho\rangle = \langle\rho\rangle_D + \langle\rho\rangle_{\mathrm{env}} \quad (8)$$

with

$$\langle\rho\rangle_D = \sum_{k=1}^{N} S_k \frac{E_{D,k}}{E_D} \rho_k^{dd}(\overrightarrow{U_s}, \overrightarrow{U_{c,k}}) \quad (9)$$

$$\langle\rho\rangle_{\mathrm{env}} = \langle\rho\rangle_{\mathrm{env},D} + \langle\rho\rangle_{\mathrm{env,diff}} \quad (10)$$

with

$$\begin{cases} \langle\rho\rangle_{\mathrm{env},D} = \sum_{k=1}^{N} \sum_{m\in V_k} S_k \frac{g_{m,k}}{\pi} \Delta S \frac{E_{D,m}}{E_D} \rho_k \rho_m \\ \langle\rho\rangle_{\mathrm{env,diff}} = \sum_{k=1}^{N} \sum_{m\in V_k} S_k \frac{g_{m,k}}{\pi} \Delta S \frac{E_{\mathrm{diff},m}}{E_D} \rho_k \rho_m. \end{cases} \quad (11)$$

This is our physical mixing model in a general case. The first term on the right-hand side of (8) gives the linear mixing of the pixel's own components ρ_k [see (9)]. The second term, which is quadratic with respect to the reflectances [see (10) and (11)], is due to the reflections from surfaces in the environment of each elementary surface. If the landscape is flat and the incident irradiance is homogeneous, the second term vanishes, and the well-known linear mixing model is obtained.

Equation (8) is valid for one wavelength and one pixel. All the irradiances depend on both wavelength and pixel location. Reflectance only depends on wavelength if it is considered Lambertian. The other terms are due to the geometrical layout and only depend on pixel location.

Note that $\sum_{k=1}^{N} S_k = 1$, but we also have another important property. The incident flux conservation at a pixel permits us to write $\Omega E_D = \sum_{k=1}^{N} d\omega_k E_{D,k}$. This leads to the following property:

$$\sum_{k=1}^{N} S_k \frac{E_{D,k}}{E_D} = 1. \quad (12)$$

This flux conservation property will be verified with simulations in the next section.

For the sake of simplicity, the reflectances in (9) are also assumed to be Lambertian hereafter. Equation (9) then becomes

$$\langle\rho\rangle_D = \sum_{k=1}^{N} S_k \frac{E_{D,k}}{E_D} \rho_k. \quad (13)$$

III. Validation of the Physical Model

In this section, a "validation" of the aforementioned model is presented using several synthetic multispectral images. These images were simulated with the 3-D radiative transfer code AMARTIS V2 [21], which is described hereafter.

A. AMARTIS Description

AMARTIS is a radiative transfer code specifically dedicated to urban areas. It allows simulating airborne and spaceborne multiangular acquisitions, in the [0.4; 2.5 μm] domain, over scenes defined by their 3-D geometry, the optical properties of every material composing the scene, the atmosphere conditions, and the viewing geometry of the sensor.

The synthetic 3-D scene is composed of uniform triangular-shape facets considered as homogeneous in terms of reflectance which can be either Lambertian or bidirectional. The atmospheric radiative properties are modeled thanks to the radiative transfer code 6S [23]. The aerosols can be modeled by the standard models of 6S, by their physical properties (with notably Junge or multimodal distributions), or directly by their optical properties (spectral optical thickness, single-scattering albedo, and phase function). The gaseous atmosphere is modeled by the standard models of 6S. AMARTIS allows the simulation of airborne or satellite sensors. The sensor is defined by the following parameters: its zenith and azimuth viewing angles defined by the optical axis orientation pointed at the center of the scene, its pixel matrix (number of pixels by rows and columns and pixel size), its spatial resolution, the wavelengths of observation, and the focal length of the instrument. The altitude of the sensor is deduced from the previous geometrical parameters.

In remote sensing, a flat-ground assumption is usually made to model the signal at ground and sensor levels. However, in cities, at very high spatial resolution, this hypothesis is no longer valid because of the complexity introduced by the relief which induced specific radiative effects. Thus, AMARTIS has been developed to overcome these limitations. It is able to model independently all the radiative contributors at ground (irradiance unit) and sensor (radiance unit) levels (Fig. 3). The

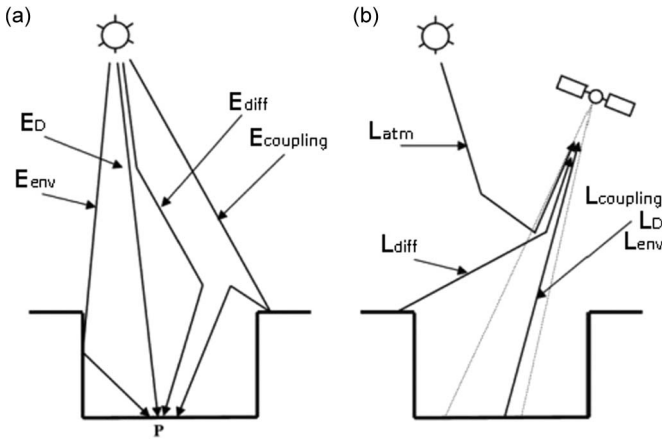

Fig. 3. Description of the different modeled radiative contributors. (a) Irradiances at the ground level. (b) Radiances at the sensor level.

irradiance at the ground level ($E_{\rm tot}$) is the sum of four components [Fig. 3(a)]: the direct irradiance (E_D), the scattered and diffused irradiance ($E_{\rm diff}$), the earth–atmosphere coupling irradiance ($E_{\rm coupling}$), and the downward-reflected irradiance ($E_{\rm env}$). The radiance at the sensor level ($L_{\rm tot}$) is the sum of the different components defined in (1) and (2) [see Fig. 3(b)]. The analytic expression of each radiative component is detailed in [21]. Due to the strong heterogeneity of the scene, $E_{\rm coupling}$, $E_{\rm env}$, and $L_{\rm env}$ are solved using ray tracing and Monte Carlo methods.

The outputs of AMARTIS are radiance images at the sensor level (total, direct, and due to the neighborhood and all other terms present in our equations) and irradiance images at the surface level (total, direct, and diffused).

The AMARTIS results are reliable and have already been validated; however, the code has two little disadvantages that can induce some artifacts in our results.

1) AMARTIS uses a Monte Carlo process to estimate the radiative terms due to reflections, which induces statistical fluctuations, essentially in shadowed areas. As this method needs a lot of photons to converge well, its convergence is less reliable in partly shadowed regions.
2) Before AMARTIS calculation, a triangulation of the 3-D scene is made. A hyperfine meshing is needed to achieve a good accuracy. Unfortunately, we are limited by computational cost and memory size, and the used mesh size often implies triangles bigger than our small elementary surfaces (three or four times bigger). This can induce some artifacts on the computed radiances, mainly around the shadow/light transitions.

B. Methodology

For each studied image at a coarse resolution X, the same image at a high resolution x is used, whose pixels would be used as the elementary surfaces k and m in our mixing model.

To validate our model, we first proceed as follows (Section III-D1).

1) Compute an image of reflectances $\langle\rho\rangle$ for pixels at a coarse resolution X [by applying our mixing model in (8), (13), (10), and (11)] using values provided at a fine resolution x for the elementary surfaces.
2) Compute the total radiance image $\langle L\rangle$ [defined in (3)] at resolution X using the obtained image of reflectances $\langle\rho\rangle$.
3) Compare our computed image $\langle L\rangle$ with the total radiance image L given by AMARTIS at resolution X.

   We then focus on $\langle L_{\rm es}\rangle$ [in (3)]. Due to (8), it can be defined as $\langle L_{\rm es}\rangle = \langle L\rangle_D + \langle L\rangle_{\rm env}$, with $\langle L\rangle_D = (\langle\rho\rangle_D/\pi)E_D t^{\uparrow{\rm es}-c}$ [with $\langle\rho\rangle_D$ defined in (13)] and $\langle L\rangle_{\rm env} = (\langle\rho\rangle_{\rm env}/\pi)E_D t^{\uparrow{\rm es}-c}$ [with $\langle\rho\rangle_{\rm env}$ defined in (10)]. [This corresponds to (2).]
4) Compare our computed image $\langle L\rangle_D$ with the radiance image L_D given by AMARTIS at resolution X. Both correspond to the solar radiance due to the solar irradiance on the surface directly reflected toward the sensor.
5) Compare $L_{\rm env}$ given by AMARTIS for the resolution X with our computed $\langle L\rangle_{\rm env}$. These terms correspond to the radiance due to the neighborhood of the considered surface (induced by reflections).

To show the discrepancy that we get when comparing our results with AMARTIS' ones, we define what we will call "errors" hereafter:

- a global absolute error in radiance units

$$\mathrm{Err}_L(Z) = \sqrt{\mathrm{mean}_i\left(\langle Z\rangle_i - Z_i\right)^2} \tag{14}$$

- a global relative error in percentage

$$\mathrm{Err}_{\%}(Z) = \sqrt{\frac{\mathrm{mean}_i\left(\langle Z\rangle_i - Z_i\right)^2}{\mathrm{mean}_i\left(Z_i^2\right)}} \times 100 \tag{15}$$

- an error in radiance units computed at a pixel i (difference between the two images)

$$\mathrm{err}_{L_i}(Z) = \left|\langle Z\rangle_i - Z_i\right|. \tag{16}$$

In all these definitions, Z stands for L, $L_{\rm env}$, or L_D, and i corresponds to a pixel in the area of interest.

In a second step, a further analysis is proposed to show the usefulness of taking into account the environment radiative component (Section III-D2).

1) Study the proportion of the terms due to the environment not only in radiances but also in reflectances (nonlinear part in the mixed reflectance).
2) Compare the importance of the term due to the direct irradiance $\langle\rho\rangle_{{\rm env},D}$ to that of the one due to the diffused irradiance $\langle\rho\rangle_{\rm env,diff}$ in reflectances [see the definitions in (11)].

We finally validate, in Section III-D3, the flux conservation property earlier discussed at the end of Section II-D.

C. Data Description

We start our analysis with simple geometric scenes; then, a synthetic urban scene is used. The images used in this study are noise free. For each studied image at a coarse resolution X, the same image at a high resolution $x = 0.2$ m is used, whose

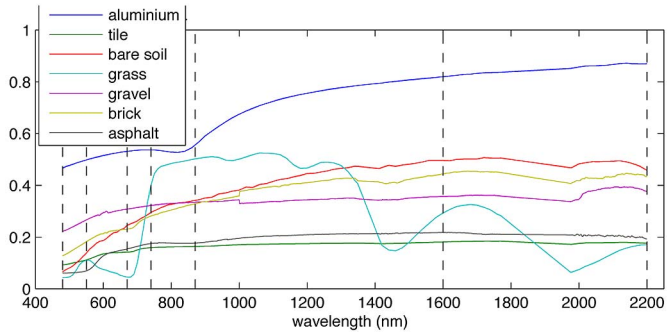

Fig. 4. Reflectance spectra of the materials present in our scenes.

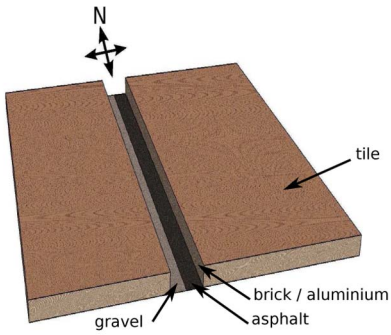

Fig. 5. Simple geometric scenes (canyon shape).

pixels would be used as the elementary surfaces k and m in our mixing model.

All used images have been generated with the following atmospheric conditions: urban aerosol model with a visibility of 23 km and midlatitude summer atmosphere.

This study concerns the reflective range (0.4–2.5 μm). The selected wavelengths are 480, 550, 670, 740, 870, 1600, and 2200 nm.

Fig. 4 shows the reflectance spectra (coming from the MEMOIRES database [24]) involved in our images. The dashed lines correspond to the seven studied wavelengths.

1) Simple Geometric Scenes: Fig. 5 represents a scene with a canyon (between two buildings), which is the most common geometrical shape in urban environments. From this scene, four images are generated. In these images, the roofs are made up of tiles, and the bottom of the canyon is covered by gravel on the left half and by asphalt on the right half. Walls are made up of bricks, except for one image where aluminum is used instead.

In order to perform a general investigation, also to see how the proportion of the nonlinear term (the contribution of the reflections on the environment of a pixel) can vary depending on the sun direction, several cases of irradiation are studied. We also aim at seeing the effect of having walls covered with aluminum instead of bricks (modern buildings are often covered with very reflective surfaces: glass, aluminum, etc.) with unchanged solar conditions. Our four images are presented in Table I, where the solar angles, the percentage of induced shadow in the canyon, and the material covering the walls are given.

TABLE I
DESCRIPTION OF THE FOUR GEOMETRIC SCENES (GENERATED FROM THE SIMPLE SCENE): SOLAR ANGLES, PERCENTAGE OF SHADOW IN THE CANYON, AND MATERIAL COVERING THE WALLS

	sun (zenith,azimuth)	shadow in the canyon	walls
C1	(16°,180°)	0%	brick
C2	(27°,239°)	20%	brick
C3	(45°,264°)	40%	brick
C4	(45°,264°)	40%	aluminium

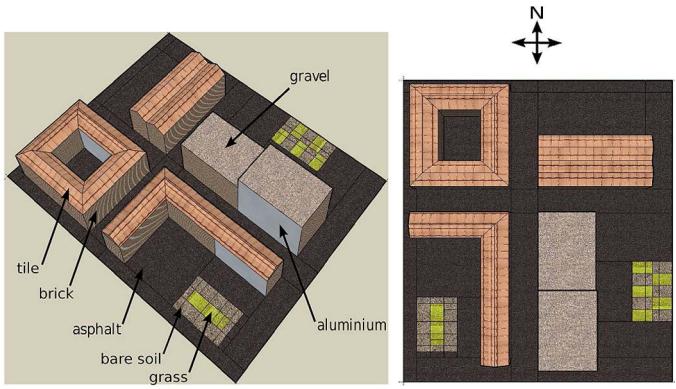

(a) Perspective view (b) Top view

Fig. 6. Urban scene. (a) Perspective view. (b) Top view.

For all these cases, the studied images have a coarse resolution of $X = 5$ m. In the coarse-resolution images, the canyon width corresponds to two 5-m pixels.

2) Urban Scene: A second more complex and realistic urban scene is also simulated (Fig. 6), which contains different kinds of building configurations that are common to European towns. The road is covered with asphalt, two small gardens include vegetation and bare soil, walls are mostly bricks with some comprising aluminum cover (the gray walls in Fig. 6), and, finally, sloped roofs are covered with tiles with flat ones covered with gravel. As the effect of solar angles is studied with the simple geometric scenes, we here consider only one configuration: $\text{solar zenith angle} = 26°$ and $\text{solar azimuth angle} = 227°$. These angles were chosen because they permit having no pixels entirely shadowed, as our model is not valid for entirely shadowed pixels.

From this scene, of size 100×80 m^2, two images with different coarse resolutions have been generated to be studied separately: one with a resolution $X = 4$ m (size 25×20 pixels) and one with a resolution $X = 5$ m (size 20×16 pixels).

Fig. 7 represents the total radiance images for this urban scene at resolutions of 0.2 and 5 m.

D. Results and Discussions

1) Global Analysis:

a) Simple geometric scenes: Results correspond to values of radiances obtained only for the pixels inside the canyon (two columns of 5-m pixels), since neighboring reflections can occur only in the bottom of the canyon, contributing then to the nonlinear term of the equivalent reflectance. In Tables II and III, the results are presented for the seven studied wavelengths.

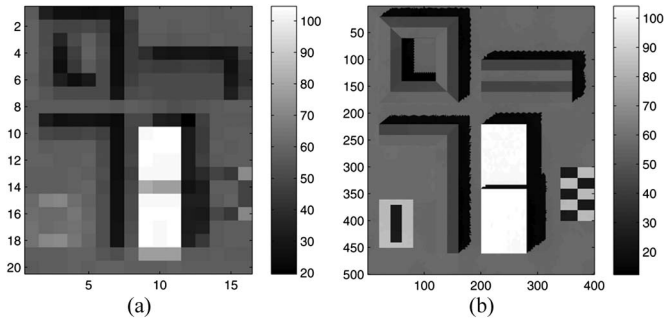

Fig. 7. Urban scene - total radiance images at resolutions of (a) 5 m and (b) 0.2 m - with a wavelength of 670 nm.

TABLE II
SIMPLE SCENES-TOTAL RADIANCES $\langle L \rangle$ (IN $\mathrm{W/m^2/sr/\mu m}$) AND ERRORS

wavelength (nm)		480	550	670	740	870	1600	2200
$\langle L \rangle$	C2	64.1	59.5	65.6	56.2	48.5	15.1	3.8
	C3	40.5	33.5	36.2	30.8	26.2	8.3	1.9
	C4	42.6	35.7	39.4	33.2	28.2	9.5	2.3
Err_L (L)	C2	0.2	0.3	0.3	0.3	0.3	0.1	0.0
	C3	0.1	0.2	0.4	0.4	0.4	0.2	0.0
	C4	0.5	0.6	0.8	0.7	0.7	0.3	0.1
$Err_{\%}$ (L)	C2	0.3	0.4	0.8	0.5	0.6	0.9	0.6
	C3	0.3	0.7	1.0	1.3	1.6	2.1	2.1
	C4	1.0	1.6	2.0	2.0	2.3	3.2	3.5

TABLE III
SIMPLE SCENES-$\langle L \rangle_{\mathrm{env}}$ (IN $\mathrm{W/m^2/sr/\mu m}$) AND ERRORS

wavelength (nm)		480	550	670	740	870	1600	2200
$\langle L \rangle_{env}$	C2	0.4	0.7	1.2	1.3	1.3	0.6	0.1
	C3	0.6	1.0	1.9	2.1	2.2	1.0	0.2
	C4	2.0	2.6	4.3	3.9	3.7	1.9	0.5
Err_L (L_{env})	C2	0.1	0.2	0.2	0.2	0.2	0.1	0.0
	C3	0.1	0.2	0.3	0.4	0.4	0.2	0.0
	C4	0.4	0.5	0.7	0.7	0.6	0.3	0.1
$Err_{\%}$ (L_{env})	C2	28	27	20	19	19	17	18
	C3	27	27	20	19	19	18	19
	C4	26	26	19	19	19	18	19

Scene C1 is not considered in these tables. As the solar irradiation direction is almost parallel to the walls, they yield no reflections in this scene. The term due to the environment is negligible, and the well-known linear model remains valid. The results show a good agreement between L and $\langle L \rangle$.

In these tables, the mean value of the radiances of interest is presented to have an idea of the global level of values. We also show the discrepancy that we get when comparing our results with AMARTIS' ones.

Table II shows that, globally, errors are very low compared to the mean values of $\langle L \rangle$ (the corresponding $\mathrm{Err}_{\%}(L)$, shown in Table II, varies globally from 0% to 3%).

To understand the source of errors, it is interesting to compare the error values Err_L in the two tables (Table II for $\langle L \rangle$ and Table III for $\langle L \rangle_{\mathrm{env}}$): They are almost the same. This means that errors seen for $\langle L \rangle$ are essentially due to errors obtained with $\langle L \rangle_{\mathrm{env}}$. Moreover, errors for $\langle L \rangle_D$ are negligible. Note that we only compute $\langle L \rangle_{\mathrm{env}}$ and $\langle L \rangle_D$ with our equations (other radiance terms are provided by AMARTIS and do not play any role in this study).

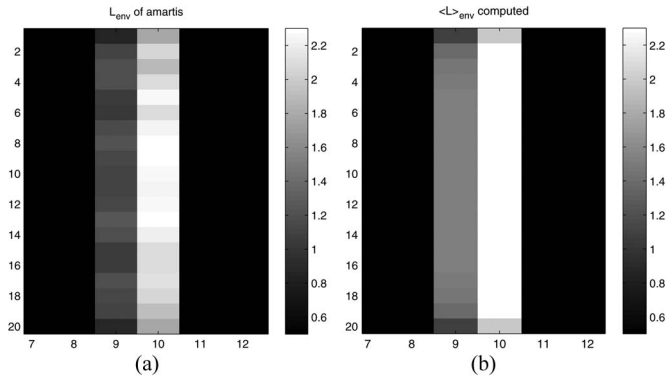

Fig. 8. Scene C3 (zoom of the canyon) - comparison of L_{env} and $\langle L \rangle_{\mathrm{env}}$ (in $\mathrm{W/m^2/sr/\mu m}$) at 670 nm. (a) L_{env}. (b) $\langle L \rangle_{\mathrm{env}}$.

We now focus on Table III. When comparing the three scenes, it can be noticed that the values of Err_L for C4 are higher than those for the other two scenes. With C3, the errors are a little higher than those for C2 (essentially when comparing with the radiance values), but the values remain close to each other. These differences in errors between the three scenes are linked to the differences for the values of $\langle L \rangle_{\mathrm{env}}$: Err_L is higher for higher values of $\langle L \rangle_{\mathrm{env}}$, whereas the percentages $(\mathrm{Err}_{\%})$ are globally stable from one scene to another.

In spite of these errors that will be explained hereafter, the results show that our model correctly describes the reflection phenomena in this simple canyon case. Indeed, the errors are, in the worst case, equal to 0.7 $\mathrm{W/m^2/sr/\mu m}$ and, in most cases, below 0.3 $\mathrm{W/m^2/sr/\mu m}$. This means that our errors are noticeably on the order of the instrumental noise level, which is about 0.2 $\mathrm{W/m^2/sr/\mu m}$ for airborne sensors (see, e.g., [25]). Therefore, most errors are reasonably weak even if errors in percentages can look high. Furthermore, most errors are due to artifacts induced by the simulation process, as explained in the following.

Fig. 8 shows an example of an image of L_{env} from scene C3, at 670 nm. The image of L_{env} (left one) can be compared with the image of $\langle L \rangle_{\mathrm{env}}$ (right one). It can be seen that there is more discrepancy for column 9 than for column 10. The obtained results, for the three scenes, showed that the errors are essentially localized in column 9 (about 33% of error), while the errors are much lower in column 10 (maximum of 13%). Note that column 9 contains a certain percentage of shadow (80% of the column area for scene C3), while in column 10, the pixels are totally irradiated by the sun. These errors are artifacts due to the AMARTIS code already explained in Section III-A.

1) The result of the Monte Carlo process in partly shadowed regions. The induced effect can be seen in the AMARTIS image [Fig. 8(a)]: The values along column 9 are not homogeneous as they should be, with fluctuations around 16% of the radiance values.
2) The scene triangulation. This induces some artifacts on the computed radiances, mainly around the shadow/light transitions. These errors can hardly be quantified. However, a simulation made on the smallest scene showed that, by increasing the number of triangles, the global error Err_L decreases by 28%.

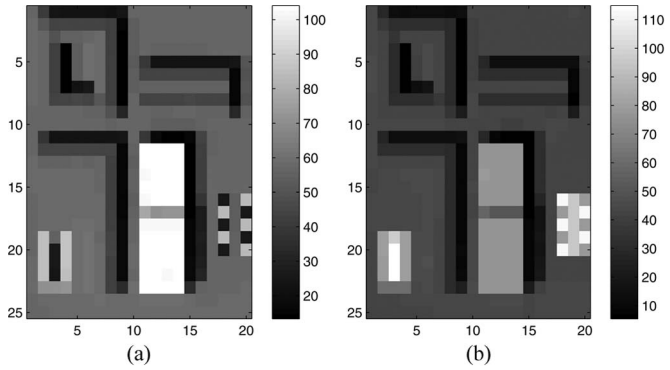

Fig. 9. Urban scene at 4-m resolution - $\langle L \rangle$ (in $\mathrm{W/m^2/sr/\mu m}$). (a) Wavelength of 670 nm. (b) Wavelength of 870 nm.

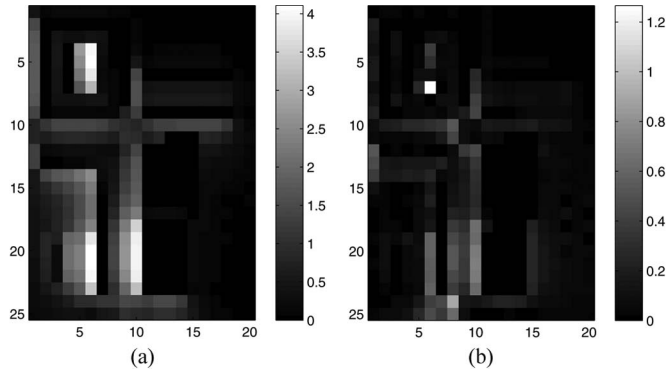

Fig. 10. Urban scene at 4-m resolution - $\langle L \rangle_{\mathrm{env}}$ and error (in $\mathrm{W/m^2/sr/\mu m}$) at 670 nm. (a) $\langle L \rangle_{\mathrm{env}}$. (b) Error: $|\langle L \rangle_{\mathrm{env}} - L_{\mathrm{env}}|$.

For these reasons, we consider that the errors mainly result from the simulation process itself rather than from our modeling. Furthermore, the errors are globally low, and if we consider that a great part of these errors are due to simulation, the residual errors become very close to the instrumental noise level. We thus consider the results as satisfactory.

b) Urban scene at 4-m resolution: The ground pixels[1] are all pure at this resolution except for the two gardens, since building dimensions have been chosen as multiples of 4 m. This will permit us to isolate the effect of reflections to better see their behavior and easily localize causes of errors. The presented results, for the urban scenes, correspond only to the pixels where $\langle L \rangle_{\mathrm{env}}$ is higher than 0.2 $\mathrm{W/m^2/sr/\mu m}$ (instrumental noise level), therefore only for the pixels where the environment plays a role.

Using the errors defined in (14) and (16), the results obtained pixel by pixel (over all the studied wavelengths) can be summarized as follows for the pixels of interest (47% of the image pixels). For L_D, the mean error $\mathrm{Err}_L(L_D)$ is equal to 0.2 $\mathrm{W/m^2/sr/\mu m}$, and for the total radiance, we have 0.3 $\mathrm{W/m^2/sr/\mu m}$. Concerning L_{env}, $\mathrm{Err}_L(L_{\mathrm{env}}) = 0.2$ $\mathrm{W/m^2/sr/\mu m}$. For this term, Fig. 11(a) shows the histogram of all obtained errors $\mathrm{err}_{L_i}(L_{\mathrm{env}})$ (over all the wavelengths). The maximum value is 1.3 $\mathrm{W/m^2/sr/\mu m}$, but 95% of the values are below 0.4 $\mathrm{W/m^2/sr/\mu m}$. The errors are globally low compared with the instrumental noise level (~ 0.2 $\mathrm{W/m^2/sr/\mu m}$).

Fig. 9 shows two images of the total radiance $\langle L \rangle$ at 670 and 870 nm. By comparing the aforementioned values of errors ($\mathrm{Err}_L \simeq 0.2$ $\mathrm{W/m^2/sr/\mu m}$ for all terms) with the radiance values in the images presented in this figure, it can be seen that the errors are generally very low.

However, some pixels yield high errors for $\langle L \rangle_{\mathrm{env}}$. In Fig. 10 are given the images of $\langle L \rangle_{\mathrm{env}}$ (left image) and the difference between the images of L_{env} and $\langle L \rangle_{\mathrm{env}}$ (right image), at 670 nm. It can be seen that most errors are low but higher errors exist for some pixels (the brightest ones). Most of these errors are due to the same reasons as detailed previously (Section III-D1a). However, another type of errors occurs in this scene, which concerns some pixels at the canyon crossings. This is due to our aggregation algorithm [when computing (8)]:

[1]Surface on the ground corresponding to the pixel projection.

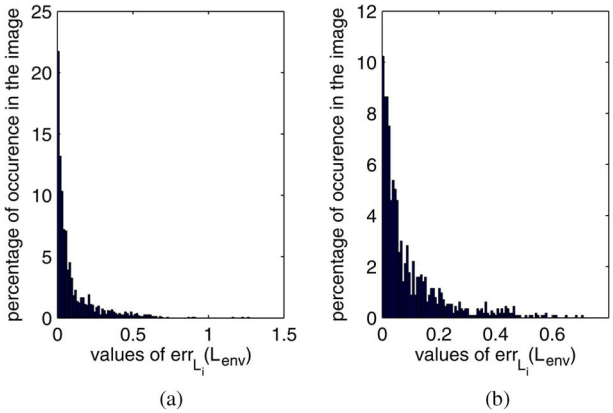

Fig. 11. Urban scenes - histograms for error $\mathrm{err}_{L_i}(L_{\mathrm{env}})$ (in $\mathrm{W/m^2/sr/\mu m}$) over all the wavelengths. (a) Four-meter-resolution image. (b) Five-meter-resolution image.

For simplification, we assumed that a surface on the ground can only receive reflections from walls of the same canyon. This induces an underestimation of $\langle L \rangle_{\mathrm{env}}$ for some pixels on the corners. The maximum error obtained in such pixels is 0.9 $\mathrm{W/m^2/sr/\mu m}$, for pixel ($\mathrm{row} = 24$, $\mathrm{col} = 8$), because we ignored their contributions due to reflections on aluminum which are not negligible. Considering the pixels around the two canyon crossings, the maximum error is 0.6 $\mathrm{W/m^2/sr/\mu m}$ for pixel ($\mathrm{row} = 10, \mathrm{col} = 8$). These errors are thus well identified, and we just have to keep in mind that they are not due to our model.

c) Urban scene at 5-m resolution: We here face a more realistic case: A ground pixel can be a mixture of two or three materials.

The global results over all the wavelengths for the pixels of interest (here, 51% of the image pixels) gave, for L, a mean error $\mathrm{Err}_L(L)$ of 0.2 $\mathrm{W/m^2/sr/\mu m}$. For L_D, we have $\mathrm{Err}_L(L_D) = 0.1$ $\mathrm{W/m^2/sr/\mu m}$. Finally, $\mathrm{Err}_L(L_{\mathrm{env}}) = 0.1$ $\mathrm{W/m^2/sr/\mu m}$. Fig. 11(b) shows the histogram of all errors $\mathrm{err}_{L_i}(L_{\mathrm{env}})$. The maximum value is here 0.7 $\mathrm{W/m^2/sr/\mu m}$, and for 95% of the pixels, the values are below 0.4 $\mathrm{W/m^2/sr/\mu m}$. Most of the error values are low compared with the level of sensor noise. Furthermore, comparing the level of the errors with the values of the total radiance faced in our images (see Fig. 12), we can note that they are globally low. Fig. 13 shows our computed image of $\langle L \rangle_{\mathrm{env}}$ (left) and the difference

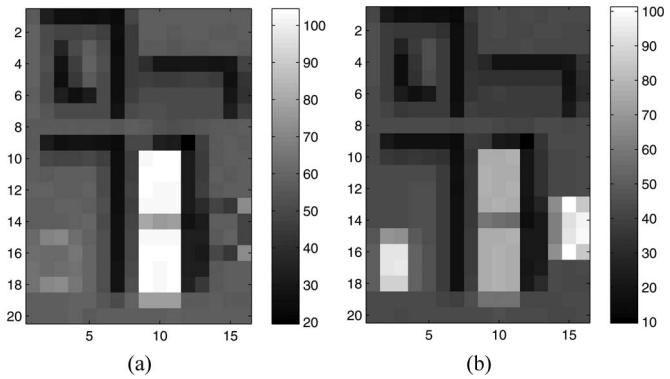

Fig. 12. Urban scene at 5-m resolution - $\langle L \rangle$ (in $\mathrm{W/m^2/sr/\mu m}$). (a) Wavelength of 670 nm. (b) Wavelength of 870 nm.

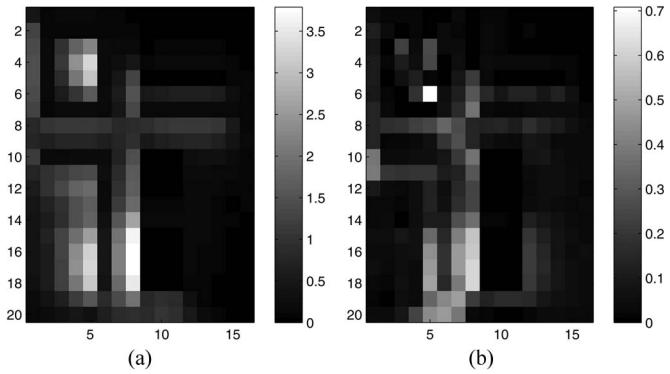

Fig. 13. Urban scene at 5-m resolution - $\langle L \rangle_{\mathrm{env}}$ and error (in $\mathrm{W/m^2/sr/\mu m}$) at 670 nm. (a) $\langle L \rangle_{\mathrm{env}}$. (b) Error: $|\langle L \rangle_{\mathrm{env}} - L_{\mathrm{env}}|$.

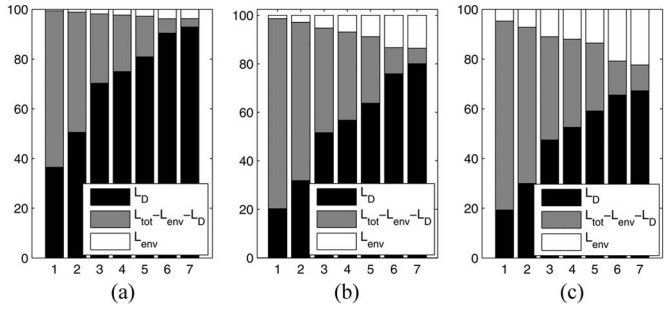

Fig. 14. Simple scenes - percentages of $\langle L \rangle_D$ and $\langle L \rangle_{\mathrm{env}}$ compared with the total radiance, for the seven studied wavelengths (in nanometers): (1) 480, (2) 550, (3) 670, (4) 740, (5) 870, (6) 1600, and (7) 2200. (a) C2. (b) C3. (c) C4.

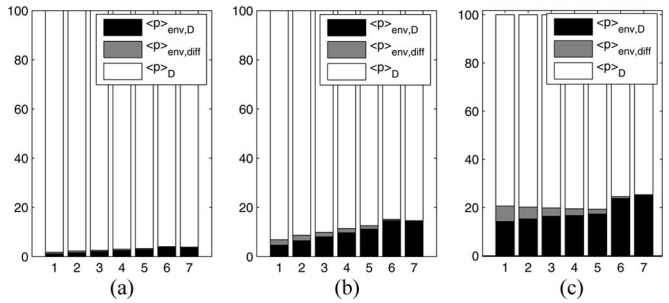

Fig. 15. Simple scenes - percentages of $\langle \rho \rangle_D$, $\langle \rho \rangle_{\mathrm{env},D}$, and $\langle \rho \rangle_{\mathrm{env,diff}}$ in the total reflectance $\langle \rho \rangle$ for the seven studied wavelengths (in nanometers): (1) 480, (2) 550, (3) 670, (4) 740, (5) 870, (6) 1600, and (7) 2200. (a) C2. (b) C3. (c) C4.

between L_{env} and $\langle L \rangle_{\mathrm{env}}$ (right), at 670 nm. The pixels with the highest errors are due to the same reasons as previously noted (in Sections III-D1a and b).

Through all these simulations, it can be concluded that the main errors are due to the generation of the synthetic scenes or to our aggregation algorithm. Moreover, these errors are comparable in level to the radiometric sensitivities of airborne sensors. We can thus consider that our model defined by (8), (13), (10), and (11) is validated.

2) Analysis of the Different Terms: In this section, we evaluate the relative importance of the terms related to the reflections using the same simulated data. For the urban scene, only the 5-m image is considered here since it is a more realistic example that includes pixel mixtures.

a) Simple geometric scenes: Fig. 14 shows that the proportion of $\langle L \rangle_{\mathrm{env}}$ depends on the sun direction (see the differences between scenes C3 and C2), which induces different levels of irradiances on the walls (higher values of irradiance when the sun direction is perpendicular to the surface). Furthermore, when the proportion of shadow increases, the amount of direct radiance is lower, so the radiance due to the environment takes a more important proportion.

The proportions of L_{env} depend also on the wavelength (L_{env} has lower importance in the blue domain). Finally, it is obvious that the materials present in the scene play an important role too (more reflections with aluminum for scene *C4* compared with scene *C3* which is characterized by the same sun direction).

Similar comments can be made concerning the proportion of $\langle \rho \rangle_{\mathrm{env}}$ in the total reflectance, presented in Fig. 15. The percentages are higher than 5% in most cases (and higher than 10% when looking only at scenes C3 and C4). Such proportions cannot be reasonably neglected in a mixing model for reflectances. We also notice that the reflections induced by the direct radiance $\langle \rho \rangle_{\mathrm{env},D}$ are more important than those induced by the diffused radiances $\langle \rho \rangle_{\mathrm{env,diff}}$ and that the latter term is almost equal to zero for wavelengths higher than 1600 nm.

b) Urban scene at 5-m resolution: In this section, we focus only on the reflectance terms, which are the terms of main concern in this paper, since the values of radiance essentially helped us to validate the model with AMARTIS. Fig. 16 contains two images that represent $\langle \rho \rangle_{\mathrm{env}}$ percentages in $\langle \rho \rangle$ for wavelengths of 670 and 870 nm. We thus can see, as previously (in Section III-D2a), that the importance of the term due to reflections depends on the materials present in the scene, on the presence of shadow, and on the area in the scene (the geometry and orientation of buildings toward the sun, etc.). It seems, e.g., obvious that $\langle \rho \rangle_{\mathrm{env}}$ is higher for pixels situated near the walls irradiated by the sun and the percentages of $\langle \rho \rangle_{\mathrm{env}}$ are higher where walls are covered with aluminum (see Fig. 6 to localize the concerned zones). Note that the white pixel in the images corresponds to a surface with a high proportion of shadow, which explains this high percentage of $\langle \rho \rangle_{\mathrm{env}}$.

Table IV shows the mean value of the percentages of $\langle \rho \rangle_{\mathrm{env}}$ as a function of the wavelength for one zone in the image:

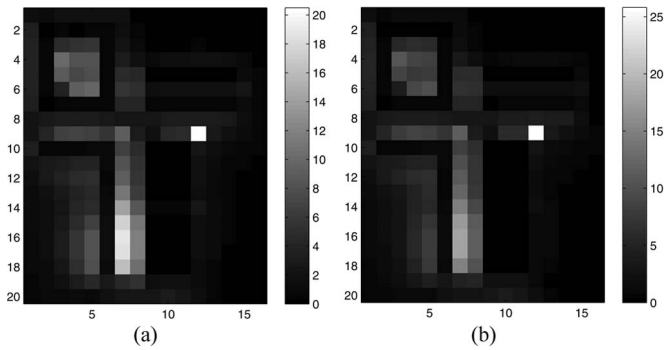

Fig. 16. Urban scene at 5-m resolution - images of the percentage of $\langle\rho\rangle_{\mathrm{env}}$ in $\langle\rho\rangle$. (a) Wavelength of 670 nm. (b) Wavelength of 870 nm.

TABLE IV
FIVE-METER URBAN SCENE-PERCENTAGES OF $\langle\rho\rangle_{\mathrm{env},D}$ AND $\langle\rho\rangle_{\mathrm{env}}$ IN $\langle\rho\rangle$, FOR ONE ZONE IN THE IMAGE (DESCRIBED IN THE TEXT)

wavelength (nm)	480	550	670	740	870	1600	2200
$\langle\rho\rangle_{env}$ (%)	8	8	10	11	11	15	14
$\langle\rho\rangle_{env,D}$ (%)	6	6	9	9	10	14	14

the canyon situated in the bottom of the image (rows 10–18 and columns 7 and 8). As previously (for the simple scenes in Section III-D2a), the importance of the term due to the environment cannot be neglected (all values higher than 5%). It can be noticed again that $\langle\rho\rangle_{\mathrm{env}}$ is less important in the blue domain. It is also clear, as for the simple scenes, that the reflections induced by the direct radiance $\langle\rho\rangle_{\mathrm{env},D}$ have the highest percentage (between 75% and 100% of $\langle\rho\rangle_{\mathrm{env}}$), and this will be useful for the next section.

3) Verification of the Flux Conservation Property: To entirely validate our model, it is necessary to verify the property of incident flux conservation, at a pixel level, cited in Section II, by validating (12). A new image at 5-m resolution is simulated, with only a part of our urban scene (rows 1–10 and columns 1–7). Taking a smaller scene permits a finer triangulation and, thus, better accuracy in the results. Note that all pixels in this image do not correspond to flat homogeneous surfaces, so the assumptions of the classical linear model are not met here. The sum-to-one property is obtained: The left-hand term of (12) has a mean value of 0.999 over the whole image and a standard deviation of 0.01. Property (12) is then true. This result is very important for the unmixing community as we will see in Section V.

IV. DERIVATION OF A SIMPLIFIED MIXING MODEL

As explained previously (in Section I), the aim of this work is to derive a mixing model for reflectances, valid in urban environments, and that could be used for spectral unmixing. However, the mixing model defined by (8), (13), (10), and (11) is not convenient yet for unmixing methods. It is a bit complicated because of the dependence of the irradiance terms on the wavelength.

By rewriting the model by highlighting the previously defined dependences of the different terms versus the 2-D pixel

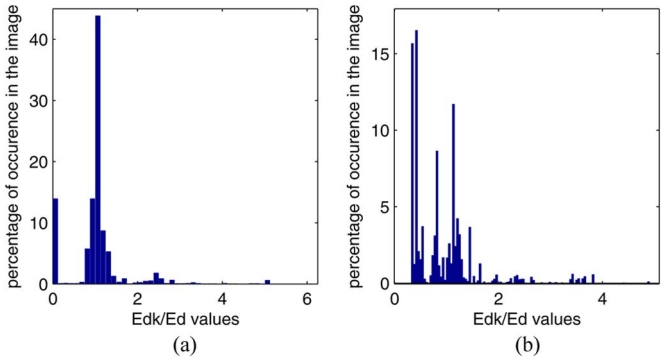

Fig. 17. Histogram of the values of $\boldsymbol{E_{D,k}}/\boldsymbol{E_D}$ in the linear and quadratic parts of our model. (a) In the linear part. (b) In the quadratic part.

position y and the wavelength λ, we have

$$\begin{aligned}\langle\rho\rangle(y,\lambda) = &\sum_{k=1}^{N} S_k(y)\frac{E_{D,k}}{E_D}(y,\lambda)\rho_k(\lambda)\\ &+\sum_{k=1}^{N}\sum_{m\in V_k} S_k(y)\frac{g_{m,k}(y)}{\pi}\Delta S\\ &\times\left(\frac{E_{D,m}}{E_D}(y,\lambda)+\frac{E_{\mathrm{diff},m}}{E_D}(y,\lambda)\right)\\ &\times\rho_k(\lambda)\times\rho_m(\lambda). \qquad (17)\end{aligned}$$

Using the source separation terminology [26]–[29] and considering wavelength-dependent sources, this model is an instantaneous (or memoryless) one since each mixture at one wavelength only depends on the sources (reflectances here) and the mixing coefficients at the same wavelength. It is a linear–quadratic model with respect to the reflectances (our sources), but the mixing coefficients include terms with a double dependence on the position and on the wavelength: the irradiance ratios (i.e., $\boldsymbol{E_{D,k}}/\boldsymbol{E_D},\ldots$). This makes the model difficult to use for unmixing. Therefore, a study of the spectral behavior of these terms is necessary to see if some simplifications are possible. To do this, we use the urban scene at 5-m resolution described in Section III.

A. Results

1) Terms $\boldsymbol{E_{D,k}}/\boldsymbol{E_D}$: Although E_D and $E_{D,k}$ depend on the wavelength, the ratios $\boldsymbol{E_{D,k}}/\boldsymbol{E_D}$ only depend on the scene geometry. As shown in [21], these terms can be reduced to ratios of cosines, so they do not depend on the wavelength.

These terms are equal to one when the surface is flat, i.e., when the linear mixing model is valid. This is not the case here because of the 3-D structures, so it is interesting to see which values can be encountered. As an example, Fig. 17 shows the histogram of the values of these ratios in our urban image, and here is a summary of the results.

- $\boldsymbol{E_{D,k}}/\boldsymbol{E_D}$ in the linear part of our model: Almost all the values are between zero and five; 54% of the values are almost equal to one (with a precision of 0.01). These terms are often different from one, which is not the case when the surface is flat.

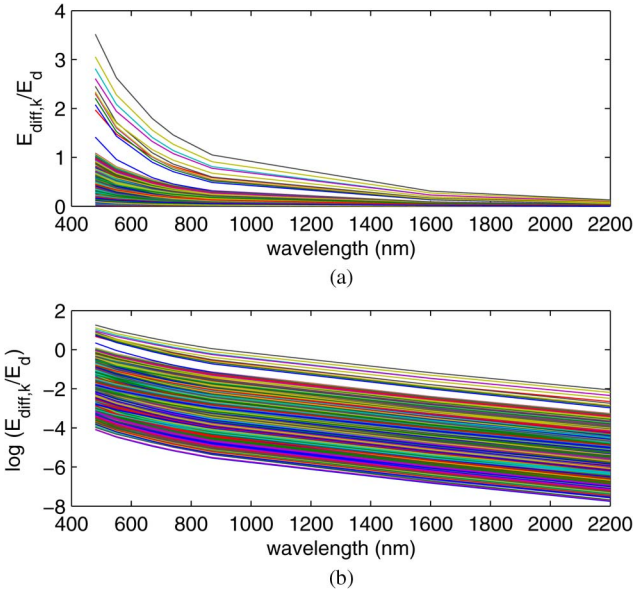

Fig. 18. (a) $E_{\mathrm{diff},m}/E_D$ versus wavelength (in nanometers). (b) $\log(E_{\mathrm{diff},m}/E_D)$ versus wavelength (in nanometers).

- $\boldsymbol{E_{D,m}/E_D}$ in the quadratic part of our model (where m here corresponds to elementary surfaces irradiated by the sun): Almost all the values are between 0.3 and 5; 94% of the values are lower than two. Note that the values are high when E_D corresponds to partially shadowed pixels.

2) Terms $\boldsymbol{E_{\mathrm{diff},m}/E_D}$: Fig. 18 graphs $\boldsymbol{E_{\mathrm{diff},m}/E_D}$ versus the wavelength for different elementary surfaces m and different pixel positions. Fig. 18(a) shows that these terms vary very slowly in the infrared domain but they significantly depend on the wavelength in the visible domain. Looking at these curves in a semilog scale [Fig. 18(b)], we can notice that all curves look like translated versions of one curve. This means that, in a linear scale, these curves are proportional. This property can be verified by computing the cross-correlation coefficients between all couples of curves, which are always higher than 0.98. We thus can approximate all our curves by one curve multiplied by a scalar factor: $u_k(\lambda) \simeq a_k v(\lambda)$, with $v(\lambda)$ being the curve chosen as a reference and $a_k = \mathrm{mean}_\lambda(u_k(\lambda)v(\lambda))/\mathrm{mean}_\lambda(v(\lambda)^2)$.

To check the proportionality of our curves, we also compute the following normalized root-mean-square error:

$$\mathrm{error} = \sqrt{\frac{\mathrm{mean}_\lambda\left(\left(u_k(\lambda) - a_k v(\lambda)\right)^2\right)}{\mathrm{mean}_\lambda\left(u_k^2(\lambda)\right)}}.$$

We obtain the following results. The maximum encountered error is 8%, and we have a mean error of 4%, for all curves. The errors are lower than 6% for more than 90% of the curves and lower than 7% for 98% of the curves. The errors obtained with this approximation are thus very low, so we can consider that these curves are almost proportional. This result is very interesting considering the fact that, whatever the materials and the geometric conditions are, the terms $\boldsymbol{E_{\mathrm{diff},m}/E_D}$ have the same spectral behavior.

B. Resulting Simplifications and the Obtained Model

The above study yields very interesting results: We have separability between the dependency of the irradiance ratios vs. the wavelength and vs. the spatial position, and $E_{D,k}/E_D$ does not depend on λ. We can thus write

$$\frac{E_{D,k}}{E_D}(y,\lambda) = \alpha_k(y) \tag{18}$$

$$\frac{E_{\mathrm{diff},m}}{E_D}(y,\lambda) = \beta_m(y) f(\lambda). \tag{19}$$

This allows us to derive a simplified mixing model from (17)

$$\begin{aligned}\langle\rho\rangle(y,\lambda) = &\sum_{k=1}^{N} S_k(y)\alpha_k(y) \times \rho_k(\lambda) \\ &+ \sum_{k=1}^{N}\sum_{m\in V_k} S_k(y)\frac{g_{m,k}(y)}{\pi}\Delta S \\ &\times (\alpha_m(y) + \beta_m(y) f(\lambda)) \times \rho_k(\lambda)\rho_m(\lambda). \end{aligned} \tag{20}$$

By grouping all coefficients depending only on the spatial position together, we finally obtain

$$\begin{aligned}\langle\rho\rangle(y,\lambda) = &\sum_{k=1}^{N} b_k(y) \times \rho_k(\lambda) + \sum_{k=1}^{N}\sum_{m\in V_k} \\ &\times (c_{k,m}(y) + d_{k,m}(y) f(\lambda)) \times \rho_m(\lambda)\rho_k(\lambda) \end{aligned} \tag{21}$$

with $b_k(y) = S_k(y)\alpha_k(y)$, $c_{k,m}(y) = S_k(y)(g_{m,k}(y)/\pi)\Delta S\alpha_m(y)$, and $d_{k,m}(y) = S_k(y)(g_{m,k}(y)/\pi)\Delta S\beta_m(y)$.

This is our general mixing model for urban environments, without notable approximation. It is a *spectrally variant* linear–quadratic model, because of the term $f(\lambda)$, in the last mixing coefficients, which still depends on the wavelength. Quantifying the error induced on $\langle\rho\rangle$ by this approximation is not easy. However, we can be sure that it is globally lower than 3%, which corresponds to the maximum expected proportion of $\langle\rho\rangle_{\mathrm{env,diff}}$ in $\langle\rho\rangle$ (see the results in Fig. 15 and Table IV).

C. Obtaining the Invariant Linear–Quadratic Model

Now, if we want to derive an *invariant* linear–quadratic model in which the sources are the reflectances, we need to neglect $f(\lambda)$ variations. As noticed in Section III, the contribution of $\langle\rho\rangle_{\mathrm{env,diff}}$ (thus the terms $E_{\mathrm{diff},m}/E_D$) in $\langle\rho\rangle_{\mathrm{env}}$ is weak compared to the contribution of $\langle\rho\rangle_{\mathrm{env},D}$ (the terms $E_{D,m}/E_D$). Therefore, the approximation that $f(\lambda)$ is constant is acceptable and can be made without important consequences. We then include $f(\lambda)$ in the definition of the term $\beta_m(y)$.

By grouping together all coefficients depending only on the spatial position, (21) becomes

$$\langle\rho\rangle(y,\lambda) = \sum_{k=1}^{N} b_k(y)\times\rho_k(\lambda) + \sum_{k=1}^{N}\sum_{m\in V_k} c_{k,m}(y)\times\rho_k(\lambda)\rho_m(\lambda) \tag{22}$$

with, here, $b_k(y) = S_k(y)\alpha_k(y)$ and $c_{k,m}(y) = S_k(y)(g_{m,k}(y)/\pi)\Delta S(\alpha_m(y) + \beta_m(y))$.

It must be clear that this simplification can be made without demonstrating the separability of the terms $E_{\mathrm{diff},m}/E_D$ versus wavelength and position (Section IV-A). The error induced by the simplification made here will be evaluated in the following section, at the pixel level.

V. Toward Spectral Unmixing

A. Final Mixing Model Adapted to Unmixing

To perform spectral unmixing or source separation, we need to have the same sources in all the image, so sources have to be independent of the pixels. In our case, the sources are the reflectances, so the model assumes that each material corresponds to only one reflectance spectrum. In (22), a reflectance is associated with each elementary surface k or m, so we regroup elementary surfaces corresponding to each material together by associating a reflectance ρ_j with each material. Our equation, for one pixel i, thus becomes a sum over all M materials

$$\langle \rho \rangle_i(\lambda) = \sum_{j=1}^{M} a_j(i) \times \rho_j(\lambda) + \sum_{j=1}^{M} \sum_{\ell=j}^{M} a_{j,\ell}(i) \times \rho_j(\lambda)\rho_\ell(\lambda) \tag{23}$$

with, for example, $a_j(i) = \sum_{k \in D_j} b_k(y)$, with D_j being elementary surfaces composed of material j. We thus have an invariant instantaneous linear–quadratic mixing model with M sources that are the reflectances of the materials present in the image. This model, already used in the literature for unmixing (see, e.g., [15]–[18]), is now justified by our physical equations.

B. Possible Assumptions About the Mixing Coefficients

The aforementioned linear–quadratic model has been used, in the literature, for unmixing, with different assumptions concerning the mixing coefficients $a_j(i)$ and $a_{j,\ell}(i)$.

In [15], it is considered that the sum of all coefficients [$a_j(i)$ and $a_{j,\ell}(i)$] is equal to one, which does not have a really physical meaning. In [16], different possibilities are proposed for $a_{j,\ell}(i)$, not justified either. The approach in [17] assumes that $a_{j,\ell}(i) = a_j(i)a_\ell(i)$, which means that a surface not seen by the sensor for the considered pixel cannot contribute by reflections to its reflectance, and this is often not true (see Fig. 20 and the discussed examples in the following).

Concerning the linear coefficients $a_j(i)$, most works keep the assumption used for the linear model [17], [18], considering that $a_j(i)$ denotes the abundances (proportion of each material in a pixel) and then

$$\sum_{j=1}^{M} a_j(i) = 1 \qquad 0 \le a_j(i) \le 1.$$

In Section II, we showed that this assumption (12) is true for our general model, i.e., even if surfaces are not flat and homogeneous. This was confirmed by simulation results in Section III-D3. In fact, we can write for a pixel i

$$\sum_{j=1}^{M} a_j(i) = \sum_{k=1}^{N} S_k \frac{E_{D,k}}{E_D} = 1.$$

For the classical linear model, which is valid when the surface is flat and homogeneous, the terms $E_{D,k}/E_D$ are equal to one, and we obtain the classical sum-to-one assumption for the abundances.

Concerning $a_{j,\ell}(i)$, related to the quadratic part of the mixing model, Fig. 19 shows a histogram of the nonzero coefficients obtained with our urban image at 5-m resolution. It may appear that most values are low (72% of the values are below 0.1), but this is normal since our urban image is, in some areas, not very representative of towns: There are no buildings on the edges of the image; thus, there are no possible multiple reflections there. Focusing on the previously chosen canyon (rows 10–18 and columns 7 and 8), the values of $a_{j,\ell}(i)$ have another distribution, which is more representative of urban environments:

1) $a_{j,\ell}(i) \in [0, 0.1]$ for 49% of the values;
2) $0.1 < a_{j,\ell}(i) < 0.2$ for 16% of the values;
3) $0.2 < a_{j,\ell}(i) < 0.25$ for 35% of them.

Next, we analyze the values of $a_{j,\ell}(i)$ for some chosen pixels in the urban image. To this end, we use the same image as in Section III-D3 (a 5-m image obtained by simulating one zone of our urban scene with a finer triangulation than that of the entire scene). Fig. 20(a) shows a 0.2-m-resolution image

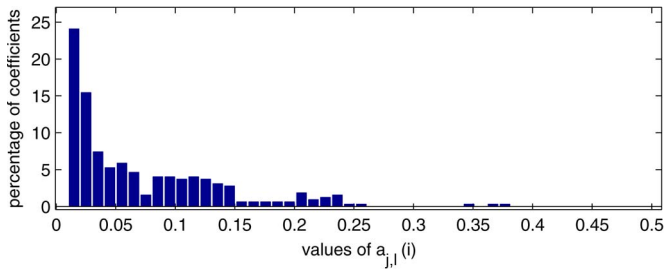

Fig. 19. Histogram of the values of $a_{j,\ell}(i)$ - urban image at 5-m resolution.

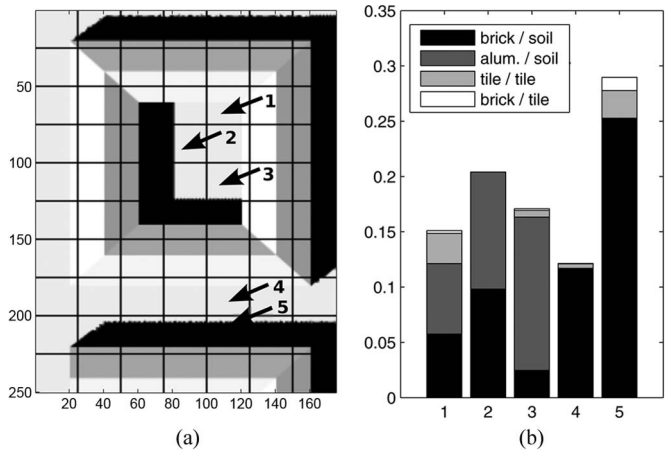

Fig. 20. Values of $a_{j,\ell}(i)$ for five chosen pixels in the used urban image [the top left corner of the image in Fig. 7(a)]. (a) E_D image, with the pixel locations. (b) Values of $a_{j,\ell}(i)$ for the five pixels.

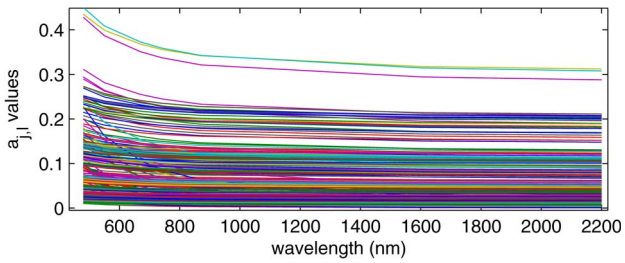

Fig. 21. Values of $a_{j,\ell}(i)$ versus wavelength - urban image at 5-m resolution.

of the used scene (image of direct irradiance E_D), with a grid showing the 5-m pixels. This figure highlights the surface orientations toward the sun and the shadowed areas (in black). The five chosen pixels are indicated. Fig. 20(b) shows the values of nonzero $a_{j,\ell}(i)$ for these pixels. As shown in the figure, these pixels have been chosen as they correspond to different configurations including shadow proportion, distance from a wall, and surface orientation (roof or soil). We can also see to which materials each coefficient corresponds (to know by which reflectances it is multiplied in the model). The aim again is to see which values can be encountered in an urban image. It is also interesting to see how the position on the scene and the proportion of the shadow can play a role on the values of $a_{j,\ell}(i)$.

- Pixel 1: There are contributions due to reflections between the roofs (tiles) and to reflections from the wall of bricks and from the wall of aluminum. However, the total coefficient is not very high since the reflections between roofs are less important than the reflections due to walls.
- Pixel 2: It corresponds to a surface more distant from the walls than the surface of pixel 1; however, the coefficient is higher than that for pixel 1. This shows again that reflections due to walls give higher contributions than reflections between roofs (pixel 1). This is due essentially to the orientation of the involved surfaces.
- Pixels 3 and 4: Pixel 3 has a high coefficient corresponding to aluminum (the wall on the right of the pixel), which is, e.g., higher than the coefficient due to the brick for pixel 4; this can be due to the surface orientation toward the sun.
- Pixel 5: The coefficient corresponding to the brick is high compared with those of other pixels, due to the presence of shadow, although the pixel is not close to the reflecting wall.

The values of $a_{j,\ell}(i)$ are certainly lower than those for the terms $a_j(i)$, but many of them cannot be neglected if we intend to perform unmixing with a good precision for urban images.

There is one last point that must be treated now: the possible error on the model induced by the approximation in Section IV-C. It has been assumed that the $a_{j,\ell}(i)$ coefficients do not depend on the wavelength. Note that the aforementioned results concerning these coefficients were obtained at the wavelength of 670 nm. Fig. 21 shows the actual variations of the terms $a_{j,\ell}(i)$ versus the wavelength. As it can be seen, the coefficients vary at the beginning of the wavelength interval but are almost stable beyond 800 nm. To see the effect of this approximation, we need to remind that assuming that the coefficients $a_{j,\ell}(i)$ are constant (versus the wavelength) corresponds to an approximation of only the term $\langle\rho\rangle_{\mathrm{env,diff}}$. This represents globally 3% in the total reflectance (see Fig. 15 and Table IV) and corresponds to 6% at most (image C4, for 480 nm). This term is thus globally low compared to the total reflectance, so the considered approximation is sufficient. Therefore, neglecting the variations of the terms $a_{j,\ell}(i)$ versus the wavelength is a reasonable assumption, and the proposed model (23) is quite accurate.

VI. Conclusion

In this paper, a mixing model for reflectances has been derived from physical equations based on the radiative transfer theory. A linear–quadratic model was thus obtained, which was validated on simulated urban images. It was demonstrated that the quadratic term cannot be neglected in urban scenes, essentially when there are many buildings and canyons (it can, e.g., range from 15% to 20% of the total equivalent reflectances). We also found that the sum-to-one property used in linear models for the coefficients is still true for the coefficients of the linear part of our model. Finally, an invariant linear–quadratic model adapted to unmixing methods was derived, with some additional information concerning the mixing coefficients. All our simulations were done without any noise. Future work will consider synthetic images with noise to analyze its impact on the importance of the terms due to the environment (quadratic terms). It would also be interesting to compare this model with the linear one while unmixing simulated urban hyperspectral images. Furthermore, we intend to validate the model with real hyperspectral images. An airborne experiment is planned in the near future over two French cities (Toulouse and Amiens) with the ONERA hyperspectral cameras HYSPEX. Finally, note that this model is true for pixels partially or totally in the sun, and it would be interesting to also derive a model for the completely shadowed pixels.

Acknowledgment

The authors would like to thank HPc-SA/RayCREATIS, provider of the Raybooster software, used in the AMARTIS simulations.

References

[1] U. Heiden, S. Roessner, K. Segl, and H. Kaufmann, "Analysis of spectral signatures of urban surfaces for their identification using hyperspectral HyMap data," in *Proc. IEEE/ISPRS Joint Workshop Remote Sens. Data Fusion Urban Areas*, 2001, pp. 173–177.

[2] N. Keshava and J. F. Mustard, "Spectral unmixing," *IEEE Signal Process. Mag.*, vol. 19, no. 1, pp. 44–57, Jan. 2002.

[3] A. Plaza, P. Martinez, R. Perez, and J. Plaza, "A quantitative and comparative analysis of endmember extraction algorithms from hyperspectral data," *IEEE Trans. Geosci. Remote Sens.*, vol. 42, no. 3, pp. 650–663, Mar. 2004.

[4] M. Parente and A. Plaza, "Survey of geometric and statistical unmixing algorithms for hyperspectral images," in *Proc. WHISPERS*, 2010, pp. 1–4.

[5] J. M. P. Nascimento and J. M. Bioucas-Dias, "Vertex component analysis: A fast algorithm to unmix hyperspectral data," *IEEE Trans. Geosci. Remote Sens.*, vol. 43, no. 4, pp. 898–910, Apr. 2005.

[6] S. Jia and Y. Qian, "Spectral and spatial complexity-based hyperspectral unmixing," *IEEE Trans. Geosci. Remote Sens.*, vol. 45, no. 12, pp. 3867–3879, Dec. 2007.
[7] R. Heylen, D. Burazerovic, and P. Scheunders, "Fully constrained least squares spectral unmixing by simplex projection," *IEEE Trans. Geosci. Remote Sens.*, vol. 49, no. 11, pp. 4112–4122, Nov. 2011.
[8] J. Silván-Cárdenas and L. Wang, "Fully constrained linear spectral unmixing: Analytic solution using fuzzy sets," *IEEE Trans. Geosci. Remote Sens.*, vol. 48, no. 11, pp. 3992–4002, Nov. 2010.
[9] X. Liu, W. Xia, B. Wang, and L. Zhang, "An approach based on constrained nonnegative matrix factorization to unmix hyperspectral data," *IEEE Trans. Geosci. Remote Sens.*, vol. 49, no. 2, pp. 757–772, Feb. 2011.
[10] J. Plaza, A. Plaza, R. Perez, and P. Martinez, "Joint linear/nonlinear spectral unmixing of hyperspectral image data," in *Proc. IEEE IGARSS*, 2007, pp. 4037–4040.
[11] W. Liu and E. Y. Wu, "Comparison of non-linear mixture models: Subpixel classification," *Remote Sens. Environ.*, vol. 94, no. 2, pp. 145–154, Jan. 2005.
[12] U. Kumar, S. K. Raja, C. Mukhopadhyay, and T. V. Ramachandra, "A multi-layer perceptron based non-linear mixture model to estimate class abundance from mixed pixels," in *Proc. IEEE Students TechSym*, 2011, pp. 148–153.
[13] R. Pu, P. Gong, R. Michishita, and T. Sasagawa, "Spectral mixture analysis for mapping abundance of urban surface components from the Terra/ASTER data," *Remote Sens. Environ.*, vol. 112, no. 3, pp. 939–954, Mar. 2008.
[14] P. Huard and R. Marion, "Study of non-linear mixing in hyperspectral imagery—A first attempt in the laboratory," in *Proc. IEEE 3rd Workshop Hyperspect. Image Signal Process.—Evol. Remote Sens.*, 2011, pp. 1–4.
[15] J. M. P. Nascimento and J. M. Bioucas-Dias, "Nonlinear mixture model for hyperspectral unmixing," in *Proc. SPIE 15th Conf. Image Signal Process. Remote Sens.*, 2009, pp. 74770I-1–74770I-8.
[16] B. Somers, K. Cools, S. Delalieux, J. Stuckens, D. V. der Zande, W. W. Verstraeten, and P. Coppin, "Nonlinear hyperspectral mixture analysis for tree cover estimates in orchards," *Remote Sens. Environ.*, vol. 113, no. 6, pp. 1183–1193, Jun. 2009.
[17] W. Fan, B. Hu, J. Miller, and M. Li, "Comparative study between a new nonlinear model and common linear model for analysing laboratory simulated forest hyperspectral data," *Int. J. Remote Sens.*, vol. 30, no. 11, pp. 2951–2962, Jun. 2009.
[18] A. Halimi, Y. Altmann, N. Dobigeon, and J.-Y. Tourneret, "Nonlinear unmixing of hyperspectral images using a generalized bilinear model," *IEEE Trans. Geosci. Remote Sens.*, vol. 49, no. 11, pp. 4153–4162, Nov. 2011.
[19] G. Fontanilles, X. Briottet, S. Fabre, S. Lefebvre, and P.-F. Vandenhaute, "Aggregation process of optical properties and temperature over heterogeneous surfaces in infrared domain," *Appl. Opt.*, vol. 49, no. 24, pp. 4655–4669, Aug. 2010.
[20] F. Becker and Z. Li, "Surface temperature and emissivity at various scales: Definition, measurement and related problems," *Remote Sens. Rev.*, vol. 12, no. 3/4, pp. 225–253, 1995.
[21] C. Miesch, X. Briottet, Y. H. Kerr, and F. Cabot, "Radiative transfer solution for rugged and heterogeneous scene observations," *Appl. Opt.*, vol. 39, no. 36, pp. 6830–6846, Dec. 2000.
[22] M. von Schönermark, B. Geiger, and H. P. Röser, *Reflection Properties of Vegetation and Soil: With a BRDF Data Base*. Berlin, Germany: Wissenschaft und Technik Verlag, 2004, ch. 2.
[23] E. F. Vermote, D. Tanre, J. L. Deuze, M. Herman, and J.-J. Morcette, "Second simulation of the satellite signal in the solar spectrum, 6S: An overview," *IEEE Trans. Geosci. Remote Sens.*, vol. 35, no. 3, pp. 675–686, May 1997.
[24] Memoires Data Base. [Online]. Available: http://www.onera.fr/dota/memoires/index.php
[25] J. A. Gómez, E. de Miguel, O. G. de la Cámara, and A. Fernández-Renau, "Status of the INTA AHS sensor," in *Proc. 5th EARSeL Workshop Imag. Spectrosc.*, Bruges, Belgium, 2007.
[26] P. Comon and C. Jutten, *Handbook of Blind Source Separation, Independent Component Analysis and Applications*. Oxford, U.K.: Academic, 2010.
[27] A. Hyvärinen, J. Karhunen, and E. Oja, *Independent Component Analysis*. Oxford, U.K.: Wiley, 2001, a volume in Series on Adaptive and Learning Systems for Signal Processing, Communications and Control.
[28] P. D. O'Grady, B. A. Pearlmutter, and S. T. Rickard, "Survey of sparse and non-sparse methods in source separation," *Int. J. Imag. Syst. Technol.*, vol. 15, no. 1, pp. 18–33, 2005.
[29] C. Jutten and J. Karhunen, "Advances in blind source separation (BSS) and independent component analysis (ICA) for nonlinear mixtures," *Int. J. Neural Syst.*, vol. 14, no. 5, pp. 267–292, Oct. 2004.

Inès Meganem received the M.Sc. degree in electronics and signal processing from ENSEEIHT, Toulouse, France, in 2009, and the Ph.D. degree in signal and image processing from the University of Toulouse, Toulouse, in 2012.

She is currently a Teaching and Research Assistant in signal and image processing with the University of Toulouse. She is also with the Office National d'Études et de Recherches Aérospatiales, Toulouse. Her main research interests concern the study of blind source separation methods for the analysis of hyperspectral images, with applications to astrophysics and spectral unmixing in remote sensing.

Philippe Déliot received the M.Sc. degree in physical engineering in 1987.

Since 1989, he has been with the Theoretical and Applied Optics Department (DOTA), Office National d'Études et de Recherches Aérospatiales (ONERA) (The French Aerospace Laboratory), Toulouse, France. He was first in charge of infrared sensor conception and realization. Since 2000, he has been working on subjects in relation with image quality in remote sensing and particularly with the calibration of an airborne system (ONERA–IGN–CNES PELICAN) and the development of a defocusing correction method for a sensor after launch (SPOT PLEIADES). He is currently involved in hyperspectral acquisition and calibration in the laboratory and airborne system implementation (SETHI). His main interests are in relation with hyperspectral image processing and its application to security and environment.

Xavier Briottet received the Ph.D. degree in electronics from the "Ecole Nationale Supérieure de l'Aéronautique et de l'Espace," Toulouse, France, in 1986 and the "Habilitation à Diriger les Recherches" from Université Paul Sabatier, Toulouse, in 1999.

In 1987, he became an Assistant Professor of signal and image processing with the "Ecole Nationale Supérieure d'Electricité," Paris, France. Since 1988, he has been with the Theoretical and Applied Optics Department (DOTA), Office National d'Etudes et de Recherches Aérospatiales, Toulouse, where he has been working on remote sensing and is currently the Director of Research in charge of the scientific politics in the department. His main research interests are radiative transfer modeling and calibration of airborne and satellite image (SPOT 1 to SPOT 5, Polder, Vegetation, and Meris) sensors in the whole optical domain using onboard devices or terrestrial targets. In radiative transfer, his studies aim to model the aggregation processes in the reflective and thermal domain over heterogeneous and rough surfaces taking into account its directional effects. He is contributing to two future space missions: MISTIGRI (multispectral thermal infrared sensor) and HYPXIM (hyperspectral sensor in the reflective domain).

Yannick Deville (M'98) was born in Lyon, France, in 1964. He received the M.Sc. degree from the École Nationale Supérieure des Télécommunications de Bretagne, Brest, France, in 1986 and the D.E.A. and Ph.D. degrees in microelectronics from the University of Grenoble, Grenoble, France, in 1986 and 1989, respectively.

From 1986 to 1997, he was a Research Scientist with Philips Research Laboratories, Limeil, France. His investigations during this period concerned various fields, including GaAs integrated microwave RC active filters, VLSI cache memory architectures and replacement algorithms, neural network algorithms and applications, and nonlinear systems. Since 1997, he has been a Professor with the University of Toulouse, Toulouse, France, where he was with the Acoustics Laboratory from 1997 to 2004. Since 2004, he has been with the Astrophysics Laboratory, Toulouse, which is part of the University of Toulouse and the French National Centre for Scientific Research (CNRS). His current major research interests include signal and image processing, higher order statistics, time–frequency analysis, neural networks, and, particularly, blind source separation methods (including independent or sparse component analysis) and their applications to remote sensing, astrophysics, quantum information processing, acoustics, and communication/electromagnetic signals.

Shahram Hosseini was born in Shiraz, Iran, in 1968. He received the B.Sc. and M.Sc. degrees in electrical engineering from Sharif University of Technology, Tehran, Iran, in 1991 and 1993, respectively, and the Ph.D. degree in signal processing from the Institut National Polytechnique de Grenoble, Grenoble, France, in 2000.

He is currently an Associate Professor with Université Paul Sabatier, University of Toulouse, Toulouse, France. His research interests include blind source separation, artificial neural networks, and adaptive signal processing.